Science Arts et Métiers
Archive Ouverte – Open Repository

Science Arts & Métiers (SAM)

is an open access repository that collects the work of Arts et Métiers Institute of Technology researchers and makes it freely available over the web where possible.

This is an author-deposited version published in: https://sam.ensam.eu
Handle ID: .http://hdl.handle.net/10985/26072

This document is available under CC BY-NC license

To cite this version :

Muthu Vignesh VELLAYAPPAN, Francisco DUARTE, Cyrille SOLLOGOUB, Justin DIRRENBERGER, Guinault ALAIN, Jessica E. FRITH, Helena C. PARKINGTON, Andrey MOLOTNIKOV, Neil CAMERON - Fabrication of Architectured Biomaterials by Multilayer Co Extrusion and Additive Manufacturing - Advanced Functional Materials - Vol. 33, n°31, - 2023

Any correspondence concerning this service should be sent to the repository Administrator : scienceouverte@ensam.eu

Arts et Métiers Institute of Technology

Exploring the possibilities of increasing energy density and efficiency in rechargeable batteries

Download this complimentary article collection

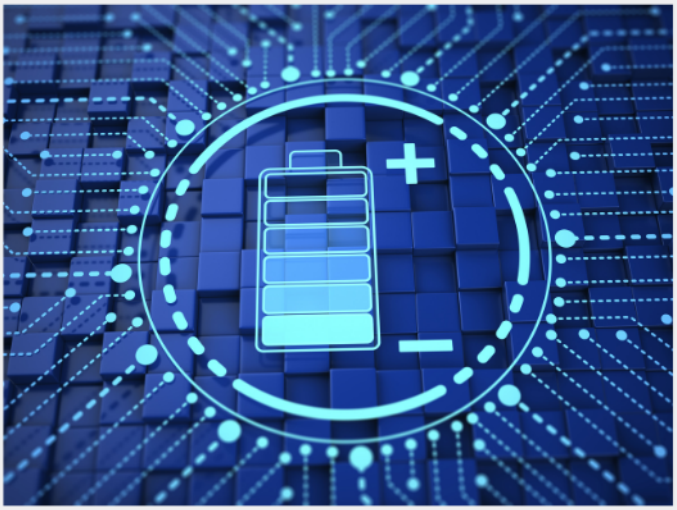

The exponential rise in the need for better, more efficient power sources has sparked an incredible amount of research into batteries. A primary focus of research has been increasing the energy density of batteries, as it allows for lighter, more portable storage of energy. Lithium-ion batteries, for example, have a much higher energy density than conventional lead-acid batteries and can be used for various purposes, such as in electric vehicles.

This article collection provides a comprehensive list of references for new methods and technologies for increasing the energy density of batteries.

Metrohm

WILEY

Check for updates

ADVANCED FUNCTIONAL MATERIALS
www.afm-journal.de

Fabrication of Architectured Biomaterials by Multilayer Co-Extrusion and Additive Manufacturing

Muthu Vignesh Vellayappan, Francisco Duarte, Cyrille Sollogoub, Justin Dirrenberger, Alain Guinault, Jessica E. Frith, Helena C. Parkington, Andrey Molotnikov, and Neil R. Cameron**

Tissue engineering benefits from advances in 3D printing and multi-material assembly to attain certain functional benefits over existing man-made materials. Multilayered tissue engineering constructs might unlock a unique combination of properties, but their fabrication remains challenging. Herein, a facile process is reported to manufacture biomaterials with an engineered multilayer architecture, via a combination of co-extrusion and 3D printing. Polymer filaments containing 5, 17, or 129 alternating layers of poly(lactic acid)/thermoplastic polyurethane (PLA/TPU) are produced, and explored for their use in fused deposition modeling (FDM) to fabricate scaffolds for cardiomyocyte culture. The co-extruded filaments exhibit a layered architecture in their cross-section with a continuous interface, and the integrity and alignment of the layers are preserved after 3D printing. The 17 alternating layers PLA/TPU composites exhibit excellent mechanical properties. It is envisaged that the multilayered architecture of the fabricated scaffolds can be beneficial for aligning cardiomyocytes in culture. It is found that the 17 alternating layers PLA/TPU significantly improve cardiomyocyte morphology and functionality compared to single phase materials. It is believed that this biomaterials fabrication scheme, combining a top-down and bottom-up approach, offers tremendous flexibility in producing a broad class of novel-architectured materials with tunable structural design for tissue engineering applications and beyond.

1. Introduction

Architectured materials are a rising class of materials resulting from an optimized spatial arrangement of multiple constituents at different microstructural scales. The architecture becomes a material parameter, allowing us to fill the gaps and push the limits of Ashby's materials performance maps.[1] Architectured materials are ubiquitous in nature, as their functional properties are commonly related to a hierarchical organization of structures at multiple scales, each exhibiting their own characteristic length and time. Such complexity results in very efficient, lightweight, smart, adaptive materials, which remain a source of inspiration for materials scientists and engineers. Studying natural materials reveals the underlying mechanisms responsible for obtaining superior properties not offered by a single material and the adaptation/mimicking of these principles helps to create enhanced synthetic materials.[2]

There are numerous examples of composite materials that exhibit a specific

M. V. Vellayappan, F. Duarte, J. E. Frith, A. Molotnikov, N. R. Cameron
Department of Materials Science and Engineering
Monash University
14 Alliance Lane, Clayton, VIC 3800, Australia
E-mail: andrey.molotnikov@rmit.edu.au; neil.cameron@monash.edu

C. Sollogoub, J. Dirrenberger, A. Guinault
PIMM
Arts et Metiers Institute of Technology
CNRS
Cnam
HESAM University
151 boulevard de l'Hopital, Paris 75013, France

The ORCID identification number(s) for the author(s) of this article can be found under https://doi.org/10.1002/adfm.202301547.

© 2023 The Authors. Advanced Functional Materials published by Wiley-VCH GmbH. This is an open access article under the terms of the Creative Commons Attribution-NonCommercial License, which permits use, distribution and reproduction in any medium, provided the original work is properly cited and is not used for commercial purposes.

DOI: 10.1002/adfm.202301547

H. C. Parkington
Department of Physiology
Biomedicine Discovery Institute
Monash University
26, Innovation Walk, Victoria 3800, Australia

A. Molotnikov
RMIT Centre for Additive Manufacturing
School of Engineering
RMIT University
Melbourne, VIC 3000, Australia

N. R. Cameron
School of Engineering
University of Warwick
Coventry CV4 7AL, UK

16163028, 0, Downloaded from https://onlinelibrary.wiley.com/doi/10.1002/adfm.202301547 by Cochrane France, Wiley Online Library on [18/04/2023]. See the Terms and Conditions (https://onlinelibrary.wiley.com/terms-and-conditions) on Wiley Online Library for rules of use; OA articles are governed by the applicable Creative Commons License

spatial arrangement of phases at macro- and micro-scales, resulting in improved material properties compared to those of the constituents considered independently.[3] Parameters related to the microstructure can thus be optimized for specific needs using a materials-by-design approach. In the field of tissue engineering, such parameters can be controlled through additive manufacturing to create architectured scaffold materials that promote the proliferation and differentiation of cells, mitigate stress concentration, or which are designed to idealize materials for model validation.[4]

Various methods have been explored over the past two decades for the fabrication of tissue engineering scaffolds, including solvent casting, thermally induced phase separation, electrospinning, batch foaming, microcellular injection molding, and additive manufacturing.[5] Additive manufacturing refers to a specific set of manufacturing technologies that produce objects/components in a bottom-up, layer-wise additive fashion directly from computer-aided designs. Such an approach to manufacturing confers benefits such as exceptional levels of achievable component complexity, bespoke, and one-off components as well as lead-time reduction compared to most other tissue engineering scaffold fabrication methods.

Surprisingly, there are no examples of the use of multilayered architectured materials as feedstocks for 3D printing.[6] In order to produce architectured materials by 3D printing, it is of prime interest to expand the set of available composite feedstocks, which currently focus on filled polymers, nanocomposites, or polymer blends.[7] Specifically, fabrication using FDM is limited to common thermoplastics and limited attempts are presented in the literature to control the microstructure of the filament at the submicron scale. The lack of control is associated with the difficulty of controlling the spatial distribution of each material in the composite filament.[5k,8]

Co-extrusion is a promising technique for creating multilayered structures, offering a simple route for the combination of properties of immiscible polymers in a stratified architecture. Combining a classical co-extrusion process with layer-multiplying elements (LMEs) allows the production of a high number (up to thousands) of alternating layers of two polymers, thus yielding individual layer thicknesses down to the micro- and nano-scale.[9] Previous studies have highlighted the benefit of such a stratification on mechanical, optical, and gas barrier properties, but its potential for tissue engineering is yet to be explored.[9b,10] Thus, using the co-extrusion process there is the potential to precisely control the size and distribution of the individual material layers in a composite filament for FDM 3D printing.

Multilayer co-extrusion allows us to manufacture architectured multilayered polymer filaments on a large scale with thousands of individual layers, which is not feasible using either conventional filament fabrication methods or by direct attachment of a co-extrusion head to the printer.[11] Since architectured materials have superior properties, they could be used as inputs/feedstocks to push the boundaries of FDM. For instance, the smallest feature size that can be produced using a conventional FDM 3D printer along the *z*-axis is 50–200 μm.[8c] Tissue engineering applications sometimes demand topographic cues at a smaller length scale to improve functionality. For example, it is increasingly recognized that surface micro and nanotopographies can be used as a powerful tool to direct the morphology and fate of cells.[12] Hence, it is anticipated that combining architectured materials and FDM may improve the functionality of the produced biomaterial. Development of new architectured composite materials for FDM requires screening in four phases, which are: filament creation from the feedstock; filament physico-chemical characterization; filament feeding and melting in the nozzle; and molten polymer deposition, road solidification, and formation of the design geometry.[13]

In this work, we explored the possibility of producing a layered polymeric composite filament of two commonly used polymeric biomaterials, poly(lactic acid) (PLA), and thermoplastic polyurethane (TPU), using a multilayer co-extrusion process, and then utilizing the resulting material for manufacturing of tissue engineering scaffolds using a FDM 3D printing approach. The combination of a top-down approach obtained with multilayer co-extrusion and a bottom-up approach achieved with additive manufacturing leads to better control of the morphology, structure, and architecture from millimeter to nanometer scales, respectively. We demonstrate that the architectured, multilayered composites obtained can have beneficial and tunable mechanical properties and can result in enhanced cardiomyocyte morphology and function compared to single-component counterparts. It is envisaged that new hybrid materials with a hierarchical structure yielding enhanced properties can be produced using this facile fabrication scheme.

2. Results and Discussion

Filament creation from the feedstock was performed using multilayer co-extrusion, utilizing the viscoelastic behavior of polymer melts under a shear field to produce a layered structure. A two-component multilayer co-extrusion system was used (**Figure 1**a) where PLA and TPU are extruded using two extruders (composition by volume of 50/50). The two polymer melts oriented into a TPU/PLA/TPU layered architecture at the feedblock. Then, the initial three-layered polymer melt flowed through several multipliers, undergoing layer multiplication at each stage. In each multiplier, the molten polymer was cut vertically into two parts, where one part flowed and spread into a top channel and the other part flowed and spread into a bottom channel (Figure 1a). Three types of multilayered filaments produced 1× PLA/TPU (1×), 3× PLA/TPU (3×), and 6× PLA/TPU (6×) constructs (Figure 1b–d), where N× represents the number of LMEs used.

A drawing of the resulting multilayered filament is presented in **Figure 2**a. The filament produced from a multilayer co-extrusion process involving 6 LMEs was not perfectly circular in cross-section (Figure 2b). However, multilayers were observed across the entire cross-sectional surface of the filament, and two distinct polymer phases were arranged in an alternating fashion, resembling an onion-like structure (Figure 2b). The higher magnification micrographs Figure 2c,d reveal clear and straight interfaces between the layers. Although immiscible, PLA/TPU blends are known to be compatible due to the interactions between PLA and the polyether composing the soft segments of TPU, with possible hydrogen bonding between the two polymers.[14] This suggests a mechanically robust multilayer material

© 2023 The Authors. Advanced Functional Materials published by Wiley-VCH GmbH

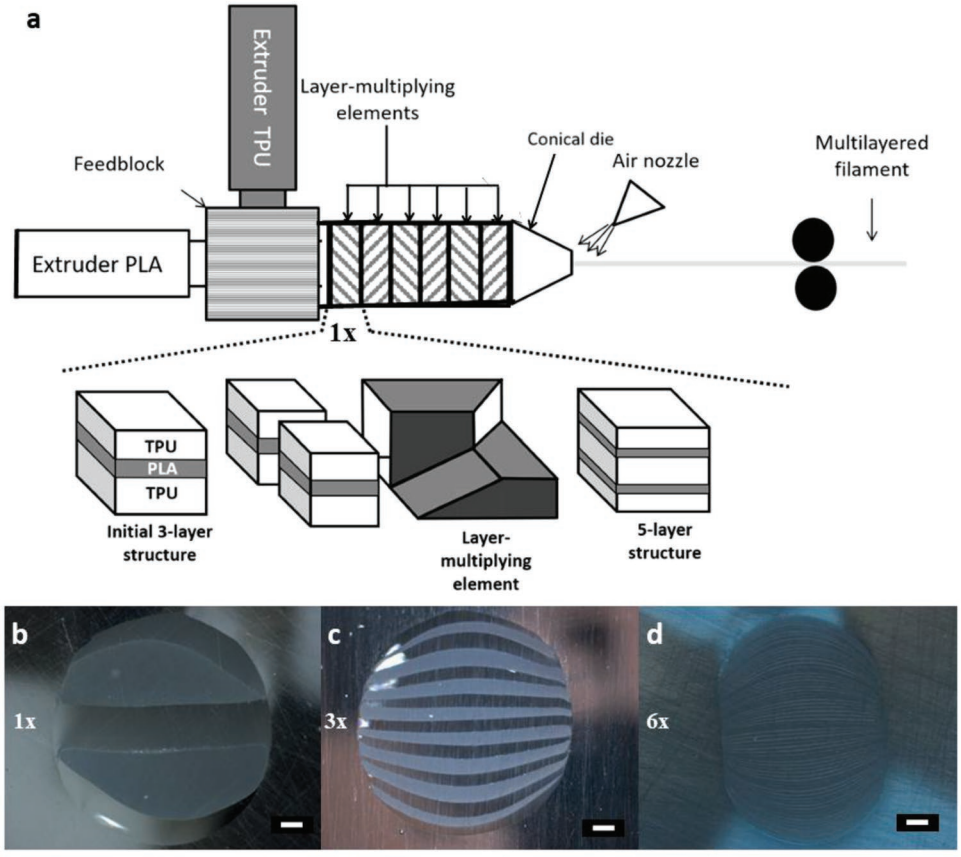

Figure 1. The fabrication of multilayer filaments using co-extrusion and linear multiplying elements. a) Schematic diagram showing the multilayer co-extrusion process by forced assembly of two polymer melts through a series of layer multiplying elements (LMEs). The expanded section shows the process for 1 multiplier (1×), which is repeated to achieve a higher number of layers; and b–d) Cross sectional surface optical micrographs of multilayered co-extruded PLA/TPU filaments produced with b) 1, c) 3, and d) 6 LMEs. Scale bar, 200 µm (b–d).

could be expected without the need for any additional compatibilizer. As expected, layering was not evident on any outer surface of the filament (Figure S1, Supporting Information).

Chemical characterization of the pure PLA and TPU filament, together with the 6x multilayer PLA/TPU, filament was performed using a combination of Raman surface mapping, Fourier-transform infrared spectroscopy (FTIR), and Raman spectroscopy. The cardinal directions north (N), south (S), east (E), and west (W) were used to represent the different sides of the outer surface of the 6× PLA/TPU filaments (Figure 2b). The Raman optical micrograph (Figure 2c) and surface mapping (Figure 2d) of the filament cross-section confirm that the layers of PLA and TPU persist in an alternating fashion. It can be concluded from the FTIR data that TPU and PLA were detected at all points on the outer surface of the multilayered PLA/TPU filament (Figure 2e). Since we performed a PLA/TPU/PLA initial co-extrusion, PLA should be in the outer surface but due to the thin external PLA layer, TPU was also detected. The FTIR peaks of PLA and TPU were sufficiently different to allow their identification. The TPU peaks in the region of 3323 cm^{-1} belonged to the N—H stretching of an aliphatic primary amine, peaks at 2938 and 2857 cm^{-1} belonged to the asymmetric and symmetric vibration of $-CH_2$ group. The peak at 1712 cm^{-1} was due to C=O stretching of ester, 1600 cm^{-1} caused by N—H bending of amine groups, 1526 and 1401 cm^{-1} representing C—N stretching and C—C absorption bands of phenyl ring in TPU.[15] Likewise for PLA, a single sharp peak at 1744 cm^{-1} resulted from C=O stretching, and peaks in the range of 1450–1375 cm^{-1} were due to C—H bending of alkane methylene groups.[11]

Figure 2f shows Raman spectra recorded in the dark and bright regions of the individual Raman microscopy image in Figure 2d. Peaks in the dark region at 1246, 1317, 1612, and 2917 cm^{-1} correspond to C—N stretching, a combination of N—H bending and C—N stretching, aromatic breathing mode vibration, and $C—H_2$ stretching.[16] These functional groups are present in TPU but not in PLA. In the bright region, characteristic peaks of PLA were observed at 1462, owing to the bending vibration of $C—H_3$. Peaks at 2944 and 2994 cm^{-1} belong to stretching vibration of $C—H_3$.[17] Studies with transmission electron microscopy (TEM) and energy-dispersive X-ray (EDX) analysis also showed distinct differences in morphology and chemical composition between PLA and TPU in the co-extruded PLA/TPU filament (Figure 2g). A nitrogen-containing group, present only in TPU, was identified only in the dark region. This evidence is consistent with the Raman surface mapping of the filament, thereby confirming that the filament cross-section consists of alternating layers of PLA and TPU.

© 2023 The Authors. Advanced Functional Materials published by Wiley-VCH GmbH

16163028, 0, Downloaded from https://onlinelibrary.wiley.com/doi/10.1002/adfm.202301547 by Cochrane France, Wiley Online Library on [18/04/2023]. See the Terms and Conditions (https://onlinelibrary.wiley.com/terms-and-conditions) on Wiley Online Library for rules of use; OA articles are governed by the applicable Creative Commons License

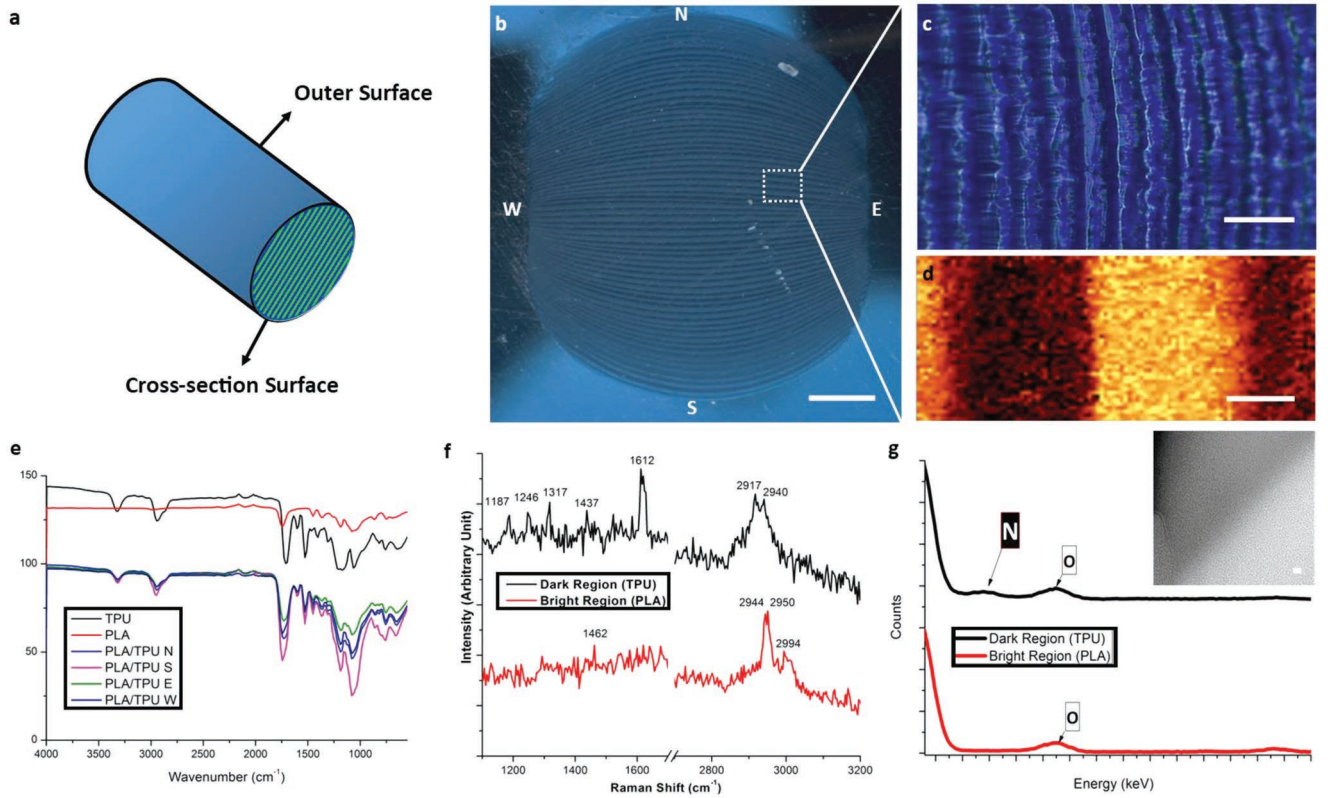

Figure 2. Physico-chemical characterization of PLA/TPU multilayer filaments. a) Drawing of PLA/TPU filament fabricated using of multilayered co-extrusion. b) Optical microscope image of a 6-multiplier PLA/TPU filament cross-sectional surface with the filament outer surface labelled according to cardinal directions North (N), East (E), South (S), and West (W), plus c) magnified cross-section surface. d) Raman optical micrograph, e) ATR-FTIR, and f) Raman spectra of the cross section surface. g) TEM image of the continuous interface region between the two polymer phases (inset) and corresponding EDX spectra of each phase. Scale bars, 100 µm (b), 60 µm (c), 7 µm (d), 100 nm (g). PLA/TPU spectra labelled N, S, E, and W in (e) were recorded in the cardinal directions identified in (b).

The evolution of the storage modulus and the loss factor (tan δ) of the filaments as a function of temperature, as determined by DMTA in tension mode, is shown in Figure S2 (Supporting Information). The storage modulus curve of PLA/TPU is present between those of PLA and TPU, as expected.[15a] Neat PLA exhibited two relaxation peaks, corresponding to the glass transition (T_g) and cold-crystallization. Neat TPU showed a relaxation peak ascribed to the T_g. The plot of the PLA/TPU co-extruded filament showed three peaks, indicating the presence of the two phases, with the T_g of TPU, T_g of PLA, and a small cold-crystallization peak of PLA at around 100 °C. The shift of the PLA T_g toward that of TPU suggests the formation of some interactions between PLA and TPU at the interfaces between the layers.

Analysis of filament feeding, melting in the nozzle, molten polymer deposition, and road solidification reveals that the PLA/TPU multilayers were preserved even after extrusion through the FDM nozzle (**Figure 3**). It was found that even at a high temperature (230 °C), the layers in the PLA/TPU filament were preserved after their extrusion through the printer nozzle. Four points in the 3D printing process were selected for further investigation. Filament feeding and melting in the nozzle, molten polymer deposition, road solidification, and formation of the design geometry (highlighted in red box Figure 3a,b). Cross-sectional SEM images at the corresponding points were obtained (Figure 3c–f). It could be seen that the layer thickness decreased gradually as the PLA/TPU filament (Figure 3c) was converted into a 3D printed PLA/TPU structure (Figure 3f). From the cross-sectional SEM images of the first portion of extruded material (Figure 3c) up to the 3D printed complex structure (Figure 3f), steady printing of PLA/TPU was observed with no mixing of the layers. The thickness of the individual polymer layers in multilayered filaments was calculated and compared with the measured thickness values to study the effect of 3D printing on the fabricated filament. Image analysis (n = 5) indicated that each layer in the PLA/TPU feedstock material was reduced from 12.0 ± 3.3 µm (calculated value 13.6 µm) before printing (Figure 3c) to 2.5 ± 0.7 µm (calculated value 3.1 µm) (Figure 3d) after extrusion and then to 2.0 ± 0.4 µm (Figure 3e) for the first stratum and ultimately to 1.7 ± 0.4 µm for an intricate structure (Figure 3f). These values are in reasonable agreement with the theoretically calculated layer thickness values given in the Methods section. For the first stratum (Figure 3e), compression and stretching exerted on the polymer melt by the nozzle head on the build platform may have reduced the total filament diameter and, simultaneously, the individual polymer layer thickness within the filament after printing. There was a further reduction in the intricate 3D printed PLA/TPU structure due to the stacking of the second stratum (Figure 3f). This phenomenon is expected

© 2023 The Authors. Advanced Functional Materials published by Wiley-VCH GmbH

16163028, 0, Downloaded from https://onlinelibrary.wiley.com/doi/10.1002/adfm.202301547 by Cochrane France, Wiley Online Library on [18/04/2023]. See the Terms and Conditions (https://onlinelibrary.wiley.com/terms-and-conditions) on Wiley Online Library for rules of use; OA articles are governed by the applicable Creative Commons License

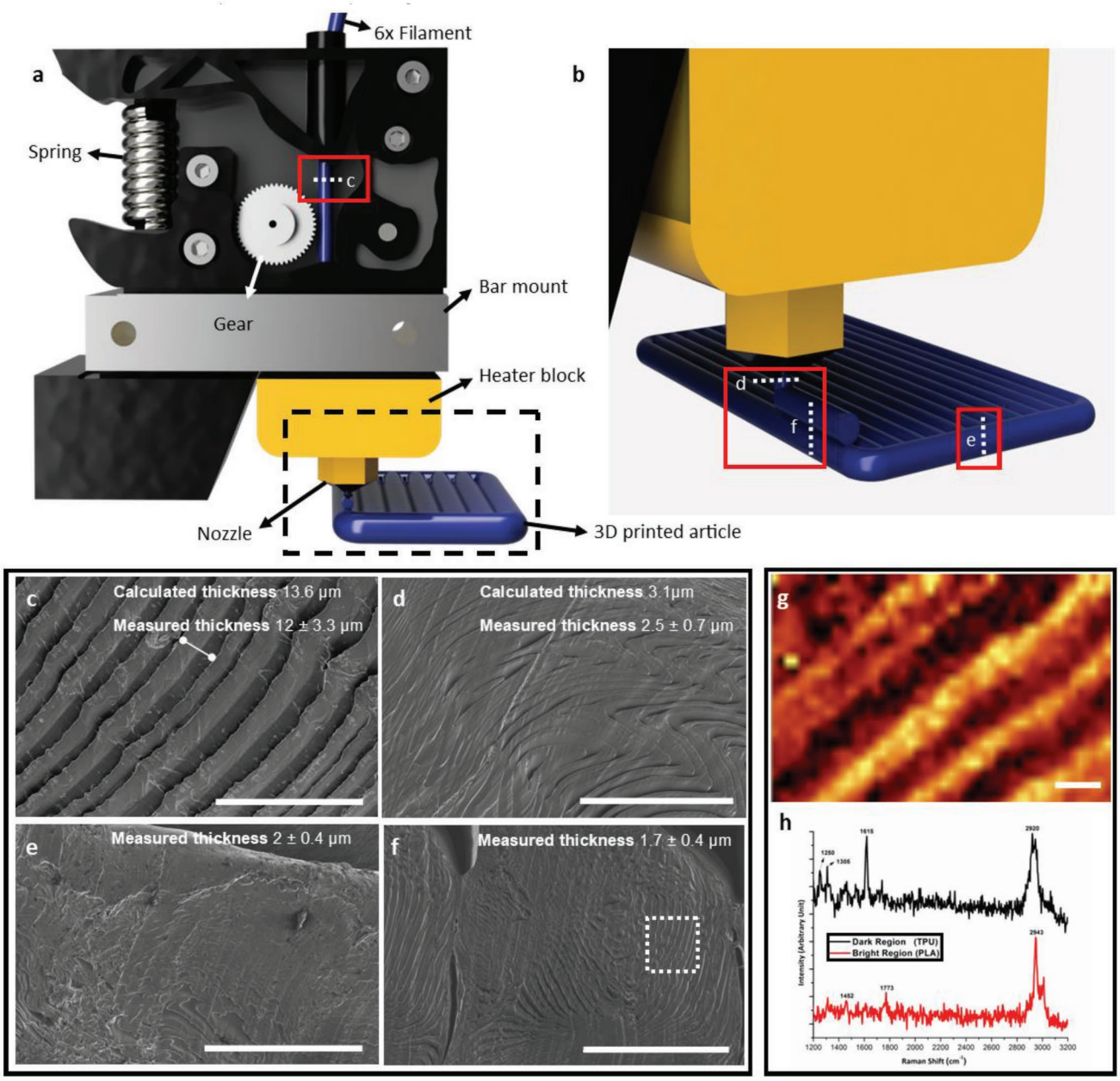

Figure 3. Morphology, structure and chemical properties of 3D printed articles from multilayered 6× PLA/TPU filaments. a) Schematic of a FDM 3D printer, 3D printing of multilayered filaments, and b) printing direction of 3D printer and illustration of the points used to examine the layering during the process (labels c, d, e, and f indicate the points where the corresponding cross-sectional SEM images were recorded). SEM images of PLA/TPU multilayer filament cross-sections before c) and after d) extrusion; e) after the first turn has been made following extrusion; and f) of the complex 3D printed structure. The dotted white box represents the imaged cross-section region. Raman optical micrograph g) and Raman spectra h) of a cross-section of the final complex 3D printed structure taken at point f of Figure 3b. Scale bars, 100 µm (c–f), 3 µm (g).

to continue until the previous stratum has cooled completely. It was also evident from the Raman mapping image in Figure 3g that the individual layer thickness in the 3D printed structure was smaller than that of the PLA/TPU filament in Figure 2d. The Raman spectral data of the 3D printed PLA/TPU cross-section (Figure 3h) further confirmed that polymer layer interleaving was avoided. Multilayering was again observed only in the printed structure cross-sectional surface whereas the top and side surfaces of the printed structure displayed no evidence of layering, identical to the virgin PLA and TPU filament. This analysis led to the conclusion that the multilayers in the PLA/TPU filament were preserved in a direction parallel to the direction of printing, with the two different polymers aligned in an alternating orientation.

Finally, the layers formed in the 3D printed biomaterials was analyzed. The overall comparison of the thickness of the polymer layers in the 1×, 3×, and 6× multilayer materials at different stages of 3D printing are given in Figure S3

© 2023 The Authors. Advanced Functional Materials published by Wiley-VCH GmbH

16163028, 0, Downloaded from https://onlinelibrary.wiley.com/doi/10.1002/adfm.202301547 by Cochrane France, Wiley Online Library on [18/04/2023]. See the Terms and Conditions (https://onlinelibrary.wiley.com/terms-and-conditions) on Wiley Online Library for rules of use; OA articles are governed by the applicable Creative Commons License

Table 1. Comparison of individual layer thickness values at different stages of 3D printing.

Number of LMEs	Total number of layers in 1.75 mm filament	Calculated individual layer thickness after extrusion [μm]	Individual layer thickness [μm][a)]	Calculated individual layer thickness after 3D printing using 0.4 mm nozzle [μm]	Individual layer thickness after 3D printing using 0.4 mm nozzle [μm][a)]
1	5	350	356 ± 158	80 μm	84 ± 19
3	17	103	103 ± 25	24 μm	24 ± 9
6	129	13.6	13 ± 2	3.1 μm	3.0 ± 0.4

[a)]Measured using ImageJ.

(Supporting Information). The calculated individual PLA/TPU layer thicknesses (**Table 1**) agree with the measured values (Figure S4, Supporting Information). For instance, 1×, 3×, and 6× filaments, had 5, 17, and 129 layers, respectively. Since these multilayers were packed within a 1.8 mm diameter filament, the 6× filament had the lowest individual layer thickness of 13.6 μm compared with 356 μm for the 1× material. It is also noteworthy that the layers were still intact without much damage to the external layer structure.

The mechanical properties of the architectured 3D printed PLA/TPU multilayered materials were investigated using tensile tests. Dog bone-shaped tensile test samples were 3D printed using the tool path shown in **Figure 4**a,b and the air gap in the cross-section of the gauge area (Figure 4c) was illustrated using Simplify3D software. The tensile results of all the 3D printed materials are shown in Figure 4d. The overall tensile properties are given in **Table 2**. Pristine PLA had a high modulus of elasticity (1000 ± 20 MPa) (n = 5) but exhibited extremely low total elongation (7.2 ± 0.6%) whereas pure TPU had a low modulus of elasticity (2.0 ± 0.1 MPa) but a high elongation at break (1568 ± 24%). It had a significantly higher elongation at break than PLA, followed by 3×, 1×, and finally 6× that showed no statistically significant increase in elongation against PLA (Figure S5, Supporting Information). The measured modulus of elasticity was higher for 1× and 3× compared to the calculated prediction obtained using the rule of mixtures (520 MPa) indicating an improvement in tensile properties due to the layered architecture.

There are two types of layers in the 3D printed samples that we have termed as macroscopic and microscopic. Macroscopic layers were formed through layer-by-layer deposition during the 3D printing process. Microscopic layers referred to the multilayers within each stratum (produced by multilayer co-extrusion). The multilayers in the feedstock filament resulted in layers within the individual deposited stratum. Since the layers run parallel to the tensile direction, stretching of pure TPU and PLA, which are bonded closely to each other, will occur. As the macro-scale bonding between filament tracks is likely to be less fused than that between the PLA and TPU layers within each stratum line, it may probably fail before the individual stratum. This failure of macro-scale bonds before failure of each stratum line could explain the phenomena observed in Figure 4e,f where all the strata came apart from one another but remained intact themselves. Due to the absence of the interfaces in the pristine PLA and TPU materials, this phenomenon was not observed in Figure 4g,h.

Finally, within each stratum, the PLA and TPU layers should respond to the external applied force according to their intrinsic properties. The PLA will fracture first, as it has a lower ductility, whilst the TPU would deform plastically once the PLA had already fractured, leading to multiple break points. Since the PLA layers within an individual stratum in the 6x multilayer material are very thin, the stress that those strata could withstand would be the force per unit area of an individual stratum multiplied by the total number of layers. However, this improved tensile property was not achieved, indicating that the inter-layer bonding could be a cause for failure.

Improvement in elongation was achieved as the number of layers was increased from 1× to 3×. Compared with 1×, an increased fracture strain from 291% to 764% was observed. This could be explained by the deformation in the samples during tensile testing.[18] In the 3× and 6× samples, crazing suppression and formation of shear bands, which is common in multilayered materials, may have occurred. This would have been followed by extension of the 3× and 6× samples through several TPU and PLA layers, which may thus have altered the overall mechanical properties.[18] Neck propagation across the entire gauge length was seen in the 3× and 6× samples. However, a significant drop from 648 to 422 MPa was seen in the tensile modulus of 6× compared with 3×. The decrease in tensile modulus could have resulted from the failure of the interface between the vertical strata (Figure 4c) rather than within the same stratum, leading to premature failure during tensile testing.

The mechanical properties of the multilayered PLA/TPU materials are different to those of conventionally produced PLA/TPU blends.[19] PLA and TPU traditional polymer blends exhibit a multiphase morphology due to the immiscible nature of the polymers, leading to weak van der Waals interactions between the phases and poor interfacial adhesion.[19–20] These two features of PLA/TPU blends result in poor mechanical properties.[19] When the 50-50 PLA/TPU blend, reported earlier, was compared against pure PLA, the drop in ultimate tensile strength value was from 62 to 17 MPa.[19] However, in the present study of multilayer materials, higher ultimate tensile strength values were observed, confirming that multilayered materials performed better than conventional blends even without any compatibilizers. For example, the ultimate tensile strength values of the 1× and 3× materials are 41 MPa and 39 MPa, respectively. Higher elongation at break was observed for PLA/TPU multilayers compared with conventional PLA/TPU blends with the same 50-50 composition.[19] In another study, the tensile strength of the PLA/TPU blend at 50-50 composition dropped from 53 MPa to 20 MPa compared to pure PLA, and elongation at break was only 4%, orders of magnitude less than the value for the 3× material (765%).[21] Thus, the overall mechanical

© 2023 The Authors. Advanced Functional Materials published by Wiley-VCH GmbH

16163028, 0, Downloaded from https://onlinelibrary.wiley.com/doi/10.1002/adfm.202301547 by Cochrane France, Wiley Online Library on [18/04/2023]. See the Terms and Conditions (https://onlinelibrary.wiley.com/terms-and-conditions) on Wiley Online Library for rules of use; OA articles are governed by the applicable Creative Commons License

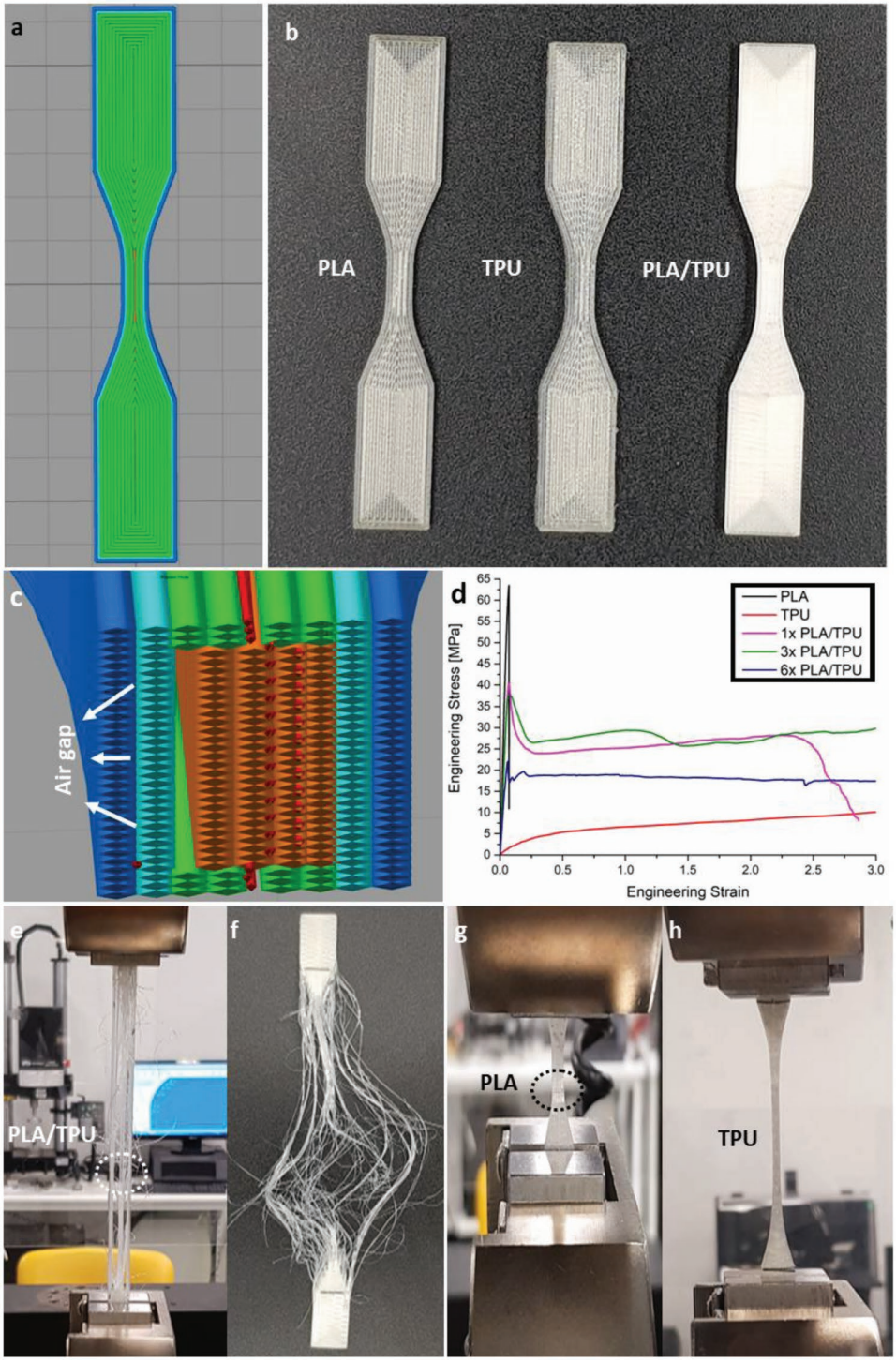

Figure 4. Investigation of the tensile properties of 3D printed samples. a) Illustration of the toolpath for 3D printing dog-bone tensile test samples, using Simplify3D software. b) 3D printed samples. c) Illustration of the air gap formed in gauge area of the tensile test samples during 3D printing, using Simplify3D software. d) Tensile data for all samples. e–h) Optical images of samples after failure.

test results observed in the present study demonstrate that multilayered PLA/TPU materials perform significantly better than conventional PLA/TPU blend composite materials.

The elastic modulus of the 1× multilayer material was higher than that of 6×, despite the lower layer thickness of 6× samples (3.1 µm) compared with 1× (80 µm). The air gap (Figure 4c) present between individual strata is likely to be a weak point, causing the sample to fail before the layers in the stratum break. The air gap may be decreased by 3D printing the tensile bars in a 90° orientation to the build platform as

© 2023 The Authors. Advanced Functional Materials published by Wiley-VCH GmbH

16163028, 0, Downloaded from https://onlinelibrary.wiley.com/doi/10.1002/adfm.202301547 by Cochrane France, Wiley Online Library on [18/04/2023]. See the Terms and Conditions (https://onlinelibrary.wiley.com/terms-and-conditions) on Wiley Online Library for rules of use; OA articles are governed by the applicable Creative Commons License

Table 2. Comparison of tensile properties of 3D printed samples.

Material	Tensile strength [MPa]	Tensile modulus [MPa]	Elongation at break [%]
PLA	63 ± 2	1000 ± 20	7.23 ± 0.6
TPU	25 ± 0.5	2.0 ± 0.06	1568 ± 24
1×	41 ± 0.3	692 ± 20.4	291 ± 20.9
3×	39 ± 0.9	648 ± 17.4	764 ± 228.9
6×	23 ± 2	422 ± 91	125 ± 64

reported in a recent study.[22] The influence of gravity during printing in a 90° orientation may help to improve the fusion of individual strata to reduce the effect of the air gap. Moreover, the outermost layer of each stratum is TPU that has a lower tensile strength. Hence, these reasons could account for reduced tensile properties of 6× samples.

The multilayer scaffolds could be beneficial for tissue engineering, because they have a layered architecture with multimaterial matrices that can be used to produce intricate mechano-structural design (to deliver physical signals such as stiffness, micro/nano-topography, etc.). Many previous studies have shown that microgrooves play a pivotal role in the alignment and structural organization of cardiomyocytes.[23] The success of cell alignment, and hence the following cell communication, is majorly dependent upon the nano- and micro-scale of the grooves, as well as their length and width and substrate material stiffness. In cardiac tissue, the contractile efficacy of cells depends on their orientation, elongation and matrix composition such as extracellular collagen.[24] Cardiomyocytes' interplay with multilayered materials by dynamic morphologic adaptation to function as an effective biomaterial was investigated. Besides improving cardiomyocytes morphology, recent studies have started to unveil the complexity of the interactions between cardiomyocytes and fibroblasts with biomaterials; as cardiomyocytes and fibroblasts are the predominant cells in the heart. Thus, to advance the cardiac tissue engineering field with multilayered biomaterials, a combination of neonatal rat cardiomyocytes and cardiac fibroblasts were used in this study.

Cardiomyocytes are well known to respond to the architecture of a biomaterial by altering the their morphology and functionality.[23b] Wettability is an important factor that can influence the ability of cells to adhere to and interact with a biomaterial surface. Cells are likely to sense the PLA and TPU polymers simultaneously in multilayered samples. The top surface of the multilayered materials (Figure S6a,b, Supporting Information) has fewer fused strands compared with the side surface (Figure S6e,f, Supporting Information) due to the layer by layer deposition of the FDM 3D printing process. The contact angle of the top surface of PLA was 68° ± 2° (Figure S6c,g, Supporting Information), while that of TPU was 109° ± 3° (Figure S6d,h, Supporting Information). Hence, PLA is more hydrophilic and can be more easily wetted by an aqueous solution compared to TPU (Figure S6i, Supporting Information). The surface energy accounts for the differences in the contact angle between PLA and TPU. TPU has a lower surface energy than PLA due to polar/dispersion interactions, resulting in a higher surface tension and contact angle.[25] The surface energy of TPU does not exceed 40 mJ m^{-2}, while PLA has a surface energy at 43.5 mJ m^{-2}.[25] The side surfaces for both samples were more hydrophobic than the top surfaces due to entrapped air bubbles (Figure S6j, Supporting Information), which might increase the contact angle.[26] Earlier studies demonstrated that most cells adhere well to hydrophilic surfaces, but adhesion depends on the nature of the cells.[27] The top hydrophilic surface of the material was chosen for cell culture experiments as the cells are more likely to attach and spread out.[27–28]

The autofluorescence of polymer scaffolds often reduces the image contrast and can interfere with cell imaging and, hence, assessment of cell functionality. Treating polymeric biomaterials materials with Sudan Black (SB) suppresses autofluorescence.[29] The autofluorescence of polymeric scaffold materials was suppressed by coating with SB (Figure S7, Supporting Information). Then, neonatal rat cardiomyocytes (NRCM) and cardiac fibroblasts were seeded at a density of 2.6×10^5 cells cm^{-2} on different scaffolds. Three days later, cell adhesion on samples was studied using scanning electron microscopy (SEM) since autofluorescence does not interfere with SEM imaging. SEM studies found no significant difference in cell adhesion between the untreated and SB-coated samples, demonstrating that SB does not adversely affect cellular behavior (data not shown). SB-coated, control glass samples and PLA had significantly more cell confluency than cells growing on TPU, while no difference was observed between glass and PLA (Figure S8, Supporting Information). Most synthetic polymers do not have functional groups that directly promote the attachment of cells. These polymers adsorb serum proteins from culture media leading to cell attachment.[30] The water contact angle of the synthetic polymers plays a crucial role in the attachment of proteins to the materials. Previous reports have suggested that cells are more likely to adhere to hydrophilic surfaces (water contact angle less than 90°). Adhesion of fibroblasts was maximum when the water contact angle of the substrate is between 60° and 80°.[31] This may explain why PLA, which has a water contact angle of 68° ± 2°, had more cell attachment compared to TPU, which has a water contact angle of 109° ± 3°.

Cell adhesion is the first and most critical requirement for cells such as NRCMs and fibroblasts to survive on a synthetic biomaterial.[27] Cell adhesion is typically followed by a series of cellular responses including cell diffusion, migration, proliferation, and differentiation. Thus, the ability of the NRCMs and fibroblasts to attach to the fabricated materials was studied first. NRCMs and cardiac fibroblasts were seeded at a density of 2.6×10^5 cells cm^{-2} on different scaffolds for 3 days. Then, cell adhesion and response to physical cues (different polymers and layer thicknesses) was studied using immunostaining and calcium imaging methods.

The ability of the different polymers to support adhesion/spreading was determined using area coverage, number of cells per image, and area coverage per cell (Figure S9, Supporting Information).[32] Glass had the highest area coverage followed by PLA and 3× samples while TPU had the smallest area coverage percentage (Figure S9a, Supporting Information). Most NRCMs were observed to attach well to glass, PLA and 6× samples, but TPU had the least NRCMs attachment (Figure S9b, Supporting Information). More cells attached to PLA compared to TPU, possibly due to PLA's lower contact

© 2023 The Authors. Advanced Functional Materials published by Wiley-VCH GmbH

16163028, 0, Downloaded from https://onlinelibrary.wiley.com/doi/10.1002/adfm.202301547 by Cochrane France, Wiley Online Library on [18/04/2023]. See the Terms and Conditions (https://onlinelibrary.wiley.com/terms-and-conditions) on Wiley Online Library for rules of use; OA articles are governed by the applicable Creative Commons License

angle value of 68° ± 2° compared to TPU that has a contact angle value of 109° ± 3°. NRCMs grown on multilayered substrates adhered well on all samples except TPU. It is particularly interesting that, in the absence of any chemical or modulus variations, as is the case for pure TPU, NRCMs failed to attach well to the TPU substrate.

The 3× samples had the highest percentage coverage per cell due to the excellent spreading of the adhered NRCMs (Figure S9c, Supporting Information). The presence of alternating PLA and TPU layers in 3× with the optimum layer thickness may have assisted the migration and spreading of the NRCMs. However, NRCMs cultured on 6× samples had the least percentage coverage per cell which may be due to the small PLA and TPU layer thickness leading to reorganization of the NRCMs cytoskeleton to smaller width thereby squeezing itself resulting in the least coverage area per cell percentage (Figure S9c, Supporting Information). Interestingly, TPU was also found to have a reasonable coverage per cell, possibly due to a lower number of cells attached but the cells looked clumped together over the TPU surface (Figure S9c, Supporting Information). The wettability of synthetic polymers affects the type, conformation, and binding strength of the proteins adsorbed from the culture medium, and thus influences cell attachment.[27] TPU is hydrophobic, so proteins such as fibronectin, vitronectin, collagen, and laminin from the culture medium are adsorbed in a denatured state, and their geometry becomes less compatible for cell binding.[27] Hence, TPU was not included in the quantitative analysis because it rarely resulted in discrete NRCMs after 3 days of culture. However, in the presence of cell-scale features, as in the case of 3× and 6×, the NRCMs adhered to the TPU segments preferentially. Since NRCMs can sense variations in matrix rigidity through a combination of muscle and non-muscle myosin contractions.[23a]

We observed cellular response to physical cues such as layer thickness by similar comparison used for the cell attachment study: PLA versus TPU, PLA versus multilayer material, and TPU versus multilayer material. Major differences were observed in the alignment of the cells between PLA and the multilayered material. The cells grew in clumps on PLA and TPU substrates (Figure 5a (i) – d(i), a(ii) – d(ii), a(iii) – d(iii)). NRCMs grew well on PLA, 1×, 3×, and 6× multilayered materials but they adopted a circular shape on TPU surfaces, which indicates a low level of cell adhesion/interaction with substrate (**Figure 5**). In the 1× samples, we did not observe any cell preference for PLA or TPU strands. No alignment or orientation was observed since the individual polymer layer thickness is large (Figure 5a(i) – a(iii)). However, starting from the 3× sample, NRCM cells seem to align along the TPU regions, as grew predominantly on the blue layers (Figure 5a(iv) – d(iv)). This was confirmed to be the TPU layer by fluorescence microscopy; autofluorescence in the blue channel was observed for pure TPU (Figure 5a(ii)) while no blue channel autofluorescence was observed for PLA (Figure 5a(i)). NRCMs tended to follow the curves of the TPU surface. When the size of the polymer layer thickness was smallest, as in the 6× samples, the NRCMs tended to become squeezed to fit on the TPU surface (Figure 5a(v) – d(v)). The interface between the PLA and TPU material phases in the multilayered scaffold may have enhanced the cells attachment to the TPU region of the multilayered material. However, the improved cell attachment/alignment commenced when the individual layer thickness of TPU was comparable to or smaller than the size of cardiomyocytes. Hence, the interfacial interactions between materials and structures are pivotal in designing of a tissue-engineered scaffold with good mechanical and biological performance.[33]

The shape of NRCMs grown on the different materials was analyzed in a quantitative manner using image analysis software CellProfiler, to investigate how NRCMs align better on the 3× and 6× TPU strands. Cell shape might be influenced by the geometrical and chemical constraints of the substrate (Figure 5e–h). The TPU-only material was not included in the following analysis because it rarely resulted in the presence of NRCMs after 3 days of culture. NRCM eccentricity increases with a decrease in the layer thickness from 1× to 6×, demonstrating contact guidance of the engineering material, causing the cells to adopt an elliptical morphology (Figure 5e). The major axis length increased from 1× to 3× (Figure 5f). This confirms that the NRCMs actively remodeled their shape to adapt to surface topography and chemistry. NRCMs cultured on 1×, 3×, and 6× samples adopted anisotropic shapes and were elongated, with a longer major axis and a shorter minor axis compared with NRCMs on the glass and PLA-only samples. The width of NRCMs, as represented by the minor axis length, corresponded to the polymer layer thickness, which was reduced from 1× to 6× samples (Figure 5g). The NRCM major axis length/width ratio is defined as the cell aspect ratio.[34] The mean aspect ratio of NRCMs was larger in samples that had a smaller layer thickness, i.e., 3× and 6× samples, as reported earlier for fibronectin coated polydimethylsiloxane (PDMS) substrates (Figure 5h).[35]

Connectivity between NRCMs grown on different substrates was investigated at day 3 in culture by immunostaining using connexin 43 (Cx43), a major cardiac gap junction protein (**Figure 6**a–f). There was some connection between adjacent NRCMs, physically ensuring inter-cellular communications. However, no significant difference in Cx43 expression of NRCMs was observed between cells grown on different substrates. These results are similar to those described in a previous report.[36] Cell alignment was also investigated by staining for troponin T, which regulates NRCM contraction following binding of calcium ions.[37] Compared with the morphology of NRCMs in the control samples (Figure 6a–c) and 1× (Figure 6d) samples, NRCMs grown on 3× (Figure 6e) and 6× samples (Figure 6f) had elongated cell shapes, oval-shaped nuclei, and appeared to align along the direction of the multilayers. The cells displayed different morphologies including spindle, sphere, square and triangle shapes on glass, PLA and 1× (Figure 6a–d) surfaces. However, on both the curved and straight regions of 3× and 6× samples, some of the NRCMs are spindle-shaped (Figure 6e,f). Spindle-shaped NRCMs are preferred in cardiac tissue engineering as the genes responsible for apoptosis and necrosis are upregulated in other cell shapes such as squares.[36,38] The relative lateral width of rat NRCMs is ≈20 μm, which matches the individual layer thickness in the 3× sample and is bigger than the layer thickness of 6×, which allows NRCMs to align and connect with nearby cells.[39]

An increase in cytoplasmic calcium triggers contraction in NRCMs.[40] Calcium transients occurred spontaneously

© 2023 The Authors. Advanced Functional Materials published by Wiley-VCH GmbH

16163028, 0, Downloaded from https://onlinelibrary.wiley.com/doi/10.1002/adfm.202301547 by Cochrane France, Wiley Online Library on [18/04/2023]. See the Terms and Conditions (https://onlinelibrary.wiley.com/terms-and-conditions) on Wiley Online Library for rules of use; OA articles are governed by the applicable Creative Commons License

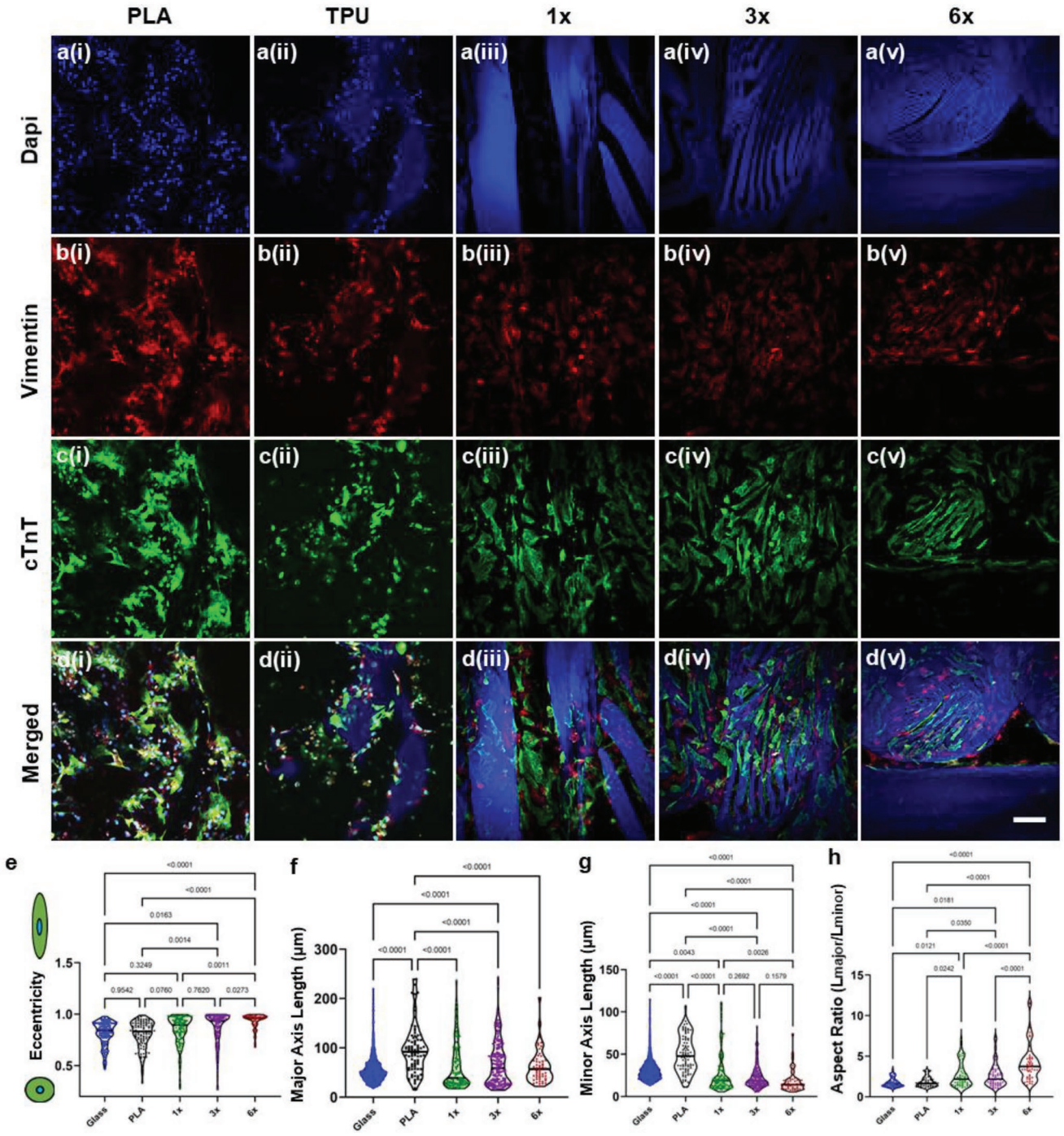

Figure 5. Qualitative and quantitative analysis of dynamic adaptation of NRCM morphology upon exposure to multilayered materials 3 days post-seeding: cell seeding density was 2.6×10^5 cells cm^{-2}, (n = 3). a(i)–d(i)) PLA, a(ii)-d(ii)) TPU, a(iii)-d(iii)) 1×, a(iv)–d(iv)) 3× and a(v)–d(v)) 6× multilayered materials. Red, fibroblast cytoskeleton (vimentin); green, NRCM actin filaments (cardiac troponin T); blue, cell nuclei (DAPI) and TPU autofluorescence. Morphometric parameters of NRCMs immunostained on scaffolds (e) eccentricity, f) major axis length, g) minor axis length, and h) cell aspect ratio. Values are expressed as mean ± SEM, (n ≥ 53). Statistical significance determined by one-way ANOVA analysis using Tukey multiple comparison test. Final overlayed image of NRCM positions and orientations in i) 1×, j) 3×, and k) 6× samples. Scale bars, 200 µm a(i)–d(v)).

in NRCMs cultured on all samples and were averaged using the Time Series ImageJ plugin (Figure 6g–k). NRCMs grown on TPU samples displayed no contraction (data not shown). Cardiomyocytes on glass (Figure 6g), PLA (Figure 6h), and 1× (Figure 6i) samples showed randomly distributed contractions. On the other hand, on 3× (Figure 6j) and 6× (Figure 6k) samples, showed frequent periods of regularly spaced oscillations in cytoplasmic calcium, with the 3× samples (Figure 6j)

© 2023 The Authors. Advanced Functional Materials published by Wiley-VCH GmbH

16163028, 0, Downloaded from https://onlinelibrary.wiley.com/doi/10.1002/adfm.202301547 by Cochrane France, Wiley Online Library on [18/04/2023]. See the Terms and Conditions (https://onlinelibrary.wiley.com/terms-and-conditions) on Wiley Online Library for rules of use; OA articles are governed by the applicable Creative Commons License

16163028, 0, Downloaded from https://onlinelibrary.wiley.com/doi/10.1002/adfm.202301547 by Cochrane France, Wiley Online Library on [18/04/2023]. See the Terms and Conditions (https://onlinelibrary.wiley.com/terms-and-conditions) on Wiley Online Library for rules of use; OA articles are governed by the applicable Creative Commons License

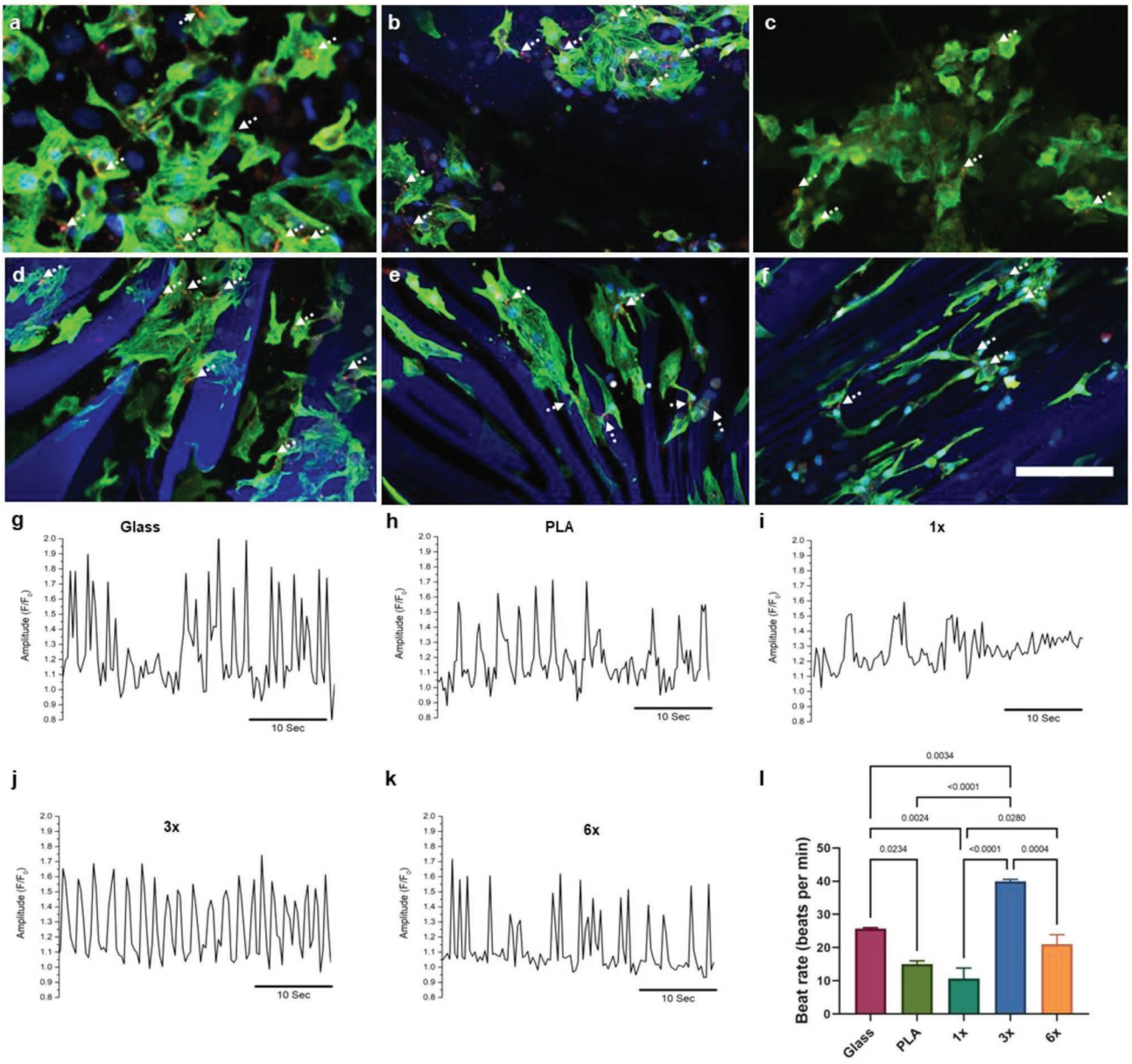

Figure 6. NRCM connection and calcium transients. Confocal microscopy images of NRCM cells immunostained on different scaffolds 3 days post-seeding: arrows represent Cx43 expression at cell seeding density of 2.6×10^5 cells cm^{-2}, (n = 3). a) Glass, b) PLA, c) TPU, d) 1×, e) 3×, and f) 6× multi-layered materials (scale bar 200 µm). Red, NRCM gap junction (Cx43); green, (cardiac troponin T); blue, cell nuclei (DAPI), and TPU autofluorescence. Comparison of averaged calcium transients of NRCMs on scaffolds 3 days post-seeding, g) glass, h) PLA, i) 1×, j) 3×, and k) 6× (n = 3) (scale bar 10 sec). Comparison of NRCM beats per minute on scaffolds 3 days post-seeding, as determined by calcium imaging (l). Values expressed as mean ± SEM, (n = 3). Statistical significance determined using one-way ANOVA analysis and Tukey multiple comparison test.

showing the most regular contractions. NRCM contractility is optimized at the cell length/width ratio observed in cells from normal hearts, and is reduced in NRCMs with morphological characteristics resembling those isolated from failing hearts.[41] The regularly spaced oscillations in cytoplasmic calcium in 3× samples corroborates a previous study that showed that increases in intracellular calcium depend on the shape of the cardiomyocyte.[41] Cell shape plays an important role in determining contractile performance of cardiomyocytes by regulating the intracellular structure and calcium handling ability.[41] Likewise, in another study, poly(glycerol sebacate) samples patterned with 20 µm channels showed improved sarcomere alignment and increased regularity of Ca^{2+} transients compared with unpatterned substrates and substrates with smaller channel patterns of 10 µm in size.[37] This further suggest that NRCMs, which have a lateral width of about 20 µm, matching the 3× layer size, may have been assisted by the multilayered material to function at an optimum level.[37] Significant differences in beats per minute (bpm) were observed between the glass and 3× samples (Figure 6l). 1× samples displayed the

© 2023 The Authors. Advanced Functional Materials published by Wiley-VCH GmbH

slowest bpm which could be due to the presence of thicker TPU layers decreasing the adhesion of fibroblasts that could assist/support NRCM attachment. The NRCMs grown on 3× samples had more intense spontaneous contractions.

Combined bioengineering strategies to manipulate cell environment are critical for the generation of adult-like NRCM in culture. One possibility for the difference between 1×/6× and 3× could be due to differences in ECM deposition and morphology characteristics on multilayered materials of different thickness may have led to varied activation of cellular signaling pathways through transmembrane integrin-like mediators.[42] Another possibility is that the degree of NRCM adhesion on the multilayered biomaterial can differentially regulate mechanosensitive responses to cell contraction followed by cytoskeletal rearrangement.[43] A third possibility is that NRCMs growing on the TPU strands may be influenced by the adjacent PLA strands in 3× and 6× multilayer 3D printed articles. This manipulation of hydrophilicity in 3× and 6× multilayer 3D printed article resulted in cylindrical NRCMs that, in turn, may have influenced cardiomyocyte phenotype, thereby improving function.[28]

The novel combination of multilayer co-extrusion and FDM fabrication allows control of the architecture of multiphase polymer systems at the micro- to nano-scale. This fabrication method opens up the possibility of producing functional biomaterials with improved functionality and tunable properties without the need for additives, chemical solvents, surface treatments, or inorganic fillers.

3. Conclusions

We present a simple and effective method for producing architectured, multilayered biomaterials composed of two immiscible polymers, PLA and TPU, through multilayer co-extrusion and additive manufacturing. Combining a ductile TPU material with brittle PLA with a specific layer thickness resulted in an architectured PLA/TPU biomaterial with improved mechanical properties, resulting in superior cardiomyocyte function compared to pristine single-phase materials. Extensive characterization of the PLA/TPU filaments indicates that the multilayers are preserved during the 3D printing process, with a continuous interphase in the cross-sectional surface of the multilayered co-extruded filaments. This work also highlights that each polymer layer thickness decreases gradually from the PLA/TPU filament to the 3D printed structure with persistent alternating alignment after 3D printing. NRCMs cultured on PLA/TPU multilayered materials expressed markers of NRCM function and cell-cell connectivity. Functional analysis of these cultures revealed synchronous and spontaneous contractions in the 3× multilayered materials.

Multilayered materials are relatively uncommon but they have multifaceted applications. Nacre (mother of pearl) is a typical example of a multilayered material found in nature. Nacre displays superior mechanical properties, such as increased toughness despite its brittle ceramic tiles and only a minor volume fraction (<5%) of soft organic phase. The metal-forming community has been inspired by naturally occurring materials and has designed processing techniques such as accumulated roll bonding that involves rolling flat sheets, cutting in half, stacking the halves together and repeating the rolling process.[44] The initial sheets can be either the same material or a combination of two different materials such as aluminum/titanium or aluminum/copper allowing the production of lighter composites with enhanced strength and ductility compared to the commercial pure materials.[45] Similarly, it has recently been pointed out that the Earth's lithosphere consists of many-layered patterns including lamellar structures, and synthetic materials that replicate these patterns may be referred to as "lithomimetic".[46] Such patterns are expected to guide the materials community to obtain materials with improved mechanical and/or functional properties.

This fabrication scheme provides a new methodology for producing architectured layered multiphase biomaterials. Although different layer thicknesses were achieved, the versatility of the co-extrusion technique could be further studied to create variations of ratios between PLA and TPU and flipped location of polymers to control the composite mechanical properties. With the same method, a filament with three polymers could also be fabricated and used for FDM 3D printing with further enhanced mechanical, gas barrier, and optical properties. In addition, there are various types of architectured materials that could be produced using gradient multilayer film processing, multilayer foam processing, and multilayer nanofiber processing.[9a] These methods could be tested to produce unique FDM filaments composed of various architectures like nanofibers, foams and gradient polymer layer thickness for a wide range of applications. X-ray-CT analysis of the samples could also be conducted to study the mechanism behind improved elongation at break of the multilayered 3D printed biomaterials. Besides that, correlation between microscale mechanical properties and layer thickness could be performed for different material combinations. Finally, the filaments can be printed in either an "out of plane" or "nonplanar" fashion to significantly access more architectured structures. The proposed fabrication scheme could also be adopted for various thermoplastic feedstock 3D printing filaments and could open up new applications ranging from biomaterials to sensors or electronics.

4. Experimental Section

Materials: Ingeo Biopolymer 2003D PLA, an extrusion grade, was purchased from Natureworks, USA. This PLA is a poly(D,L-lactide) with a percentage of D-lactic acid units of 4.3%. Its melt temperature is ≈160 °C, with a melt index of 6 g/10 min as given by Natureworks. The molecular weight as determined by SEC was $M_w \approx 210\,000$ g mol^{-1} with a dispersity ($Đ$) value of 2.1. Elastollan C90A TPU, purchased from BASF, Germany, is an extrudable thermoplastic polyurethane, with a melt index of 30–50 g/10 min.

Multilayer Co-Extrusion and 3D Printing: The multilayer PLA/TPU filament was fabricated using a traditional 3-layer structure. The feedblock was used to shape and combine the molten PLA and TPU polymers entering from the adapter into well-defined polymer stacks for delivery to the flat die. The PLA and TPU melt-orient into an A/B/A layer architecture at the feedblock. As the 3-layer co-extruded polymer melt was passed through a series of layer-multiplying elements (LME), the layers were multiplied based on Baker's transformation [130]: the melt was cut into half vertically then each half was compressed and

© 2023 The Authors. Advanced Functional Materials published by Wiley-VCH GmbH

16163028, 0, Downloaded from https://onlinelibrary.wiley.com/doi/10.1002/adfm.202301547 by Cochrane France, Wiley Online Library on [18/04/2023]. See the Terms and Conditions (https://onlinelibrary.wiley.com/terms-and-conditions) on Wiley Online Library for rules of use; OA articles are governed by the applicable Creative Commons License

re-stretched until it achieved its original width. The weight composition of PLA and TPU was set as 50/50 wt.% by adjusting the speed of the single-screws (10 rpm for PLA and 11 rpm for TPU) and controlled gear pumps. PLA and TPU pellets were fed in the hoppers separately; then were melted in the single screw extruders and were combined in the mixing block. The complete setup used for this experiment is shown in Figure 2. The shape of the extruded polymers was also checked before adding the die to confirm that the multilayers are stable before it enters into the 2.0 mm die to result in PLA/TPU filament. The temperature of the feed-block (180 °C), barrel/mixing section (190 °C for TPU and 200 °C for PLA) and the conical die was set to 210 °C after purging the entire system for almost an hour with polyethylene to remove impurities.

The 3D objects printed in this study were produced using the following workflow: STL data produced in the Solidworks program (2017 version) was sliced using the Simplify3D software. The resulting G-code was later 3D printed using a commercially available FlashForge Creator Pro 3D FDM 3D printer using the optimized printing parameters.

Morphology and Characterization: DMTA tests were carried out both on the multilayered filaments and the printed samples using a TA Q800 apparatus, working in a dynamic tensile mode for multilayered filaments and dual cantilever mode for printed samples, on small bar samples (60 mm length, 13 mm width, and 5 mm thickness). The frequency was set at 1 Hz and the imposed deformation at 1%. The samples were heated from 25 to 180 °C at a heating rate of 2 °C min^{-1}. At least two samples were tested to average the results obtained.

The morphology of PLA, TPU, PLA/TPU filaments, and 3D printed structures of each type of filament was observed under Nikon Eclipse Light Microscope and a high resolution SEM (FEI Nova NanoSEM 450 FEGSEM). Cross-sectional SEM images were obtained at a series of locations starting from the PLA/TPU filaments before extrusion, after extrusion, followed by a turn in printing to intricate structure. This procedure is required to investigate that the multilayered PLA/TPU printing results in uniform layers and corroborate that the multilayers persist even after printing for a prolonged period of time.

The produced PLA, PLA/TPU (1×, 3×, and 6×) filaments and 3D printed structures were embedded in epoxy resin at 25 parts with 3 parts of hardener. Then the resin was cured for 3 days before polishing. The filaments were placed horizontally and vertically in the mold to obtain cross-section and side-section views of the filaments after polishing. Mecatech 334 polishing machine with silicon carbide paper was used for polishing. After polishing, samples were observed under dark field optical microscope at 5×, 10×, and 20×.

For SEM, sample cross-section was obtained by cutting meticulously using carbon steel surgical blades sterilized by gamma irradiation. The samples were mounted vertically in a suitable cross-section stub and were iridium-coated using Cressington 208 HR sputter coater. Imaging was performed at 3 kV using secondary electron mode and Everhart-Thornley detector with a working distance ranging from 5 to 6 mm. For TEM, a thin section (≈150 nm) was ultramicrotomed from a bulk PLA/TPU sample using a diamond knife followed by "lift out" onto a copper grid. TEM imaging and elemental analysis based on EDX was performed using FEI Tecnai G2 T20 TEM at an accelerating voltage of 20 kV. Three points were chosen randomly in the bright and dark regions at magnification of 5000X where the EDX spectrum was collected, processed and compared.

Nicolet 6700 ATR-FTIR (ThermoFisher Scientific, Madison, WI, USA) with infrared source, number of sample scans 32, and resolution 4 cm^{-1} was used to determine the composition of PLA and TPU in PLA, TPU, and PLA/TPU 3D printing filaments. In the multilayered co-extruded PLA/TPU filaments, mid-points of the filament on all four sides were marked as north, east, south, and west and then corresponding FTIR spectra were acquired. The resultant FTIR spectra of PLA, TPU, and PLA/TPU samples were base-line corrected, processed and the graphs were stacked using Ominic 8.0 software. Each FTIR spectrum was then compared with corresponding SEM surface images at the same points.

Raman image scanning was performed using a Raman microscope (WITec GmbH, USA) with a laser wavelength of 532 nm. Image scan width and height were chosen as 20 µm and 10 µm, respectively with the scan area comprising 50 points per line and 25 lines per image. Chemical mapping was performed by selecting the center of mass at the Raman shift range of 2850–3050 rel.1 cm^{-1}. The Raman peak values at selected regions from the chemical mapping image were exported to .txt format using the WITec GmbH Project Management tool, processed, and plotted using OriginPro 9.1 software.

Tensile mechanical testing was performed on 3D printed tensile bars using Instron 4505 tensile machine under dry conditions, following the standard ASTMD638 test method for tensile properties of plastics. The tests were performed at an ambient temperature of 23 °C with a crosshead speed of 1 mm min^{-1}.

FDM 3D printing of a rectangle was performed. The water contact angle of the 3D printed PLA and TPU samples was measured at the top and side surface of the PLA and TPU using the sessile-drop method.[47] The contact angle instrument was composed of a sample stage to hold the 3D printed substrate, a syringe to apply a droplet of deionized water, a light source on the back and a camera to capture the profile of the water drop on the 3D printed PLA and TPU. A water-drop with a volume of 50 µL was placed on the samples and then allowed for 30 s to stabilize. An image of a liquid droplet on a solid substrate was captured. Then, the angle formed between the liquid–solid interface was measured by the SCA20 software.

Autofluorescence of all the 3D printed samples in the red, blue and green region was quenched using Sudan black as described previously.[29] 0.1% concentration Sudan black solution was prepared by dissolving SBB powder (Sigma-Aldrich) in 70% (v/v) ethanol, and syringe-filtered (0.2 µm) at 50 RPM rocker. The 3D printed samples were then immersed in the SBB solution overnight at 4 °C. After staining, the samples were rinsed in 1×phosphate-buffered saline (PBS; Fisher Scientific) thrice and exposed to UV light overnight for sterilisation.

Layer Thickness Calculation: The thickness of individual layers in the cross-sectional SEM images was determined using ImageJ software (version 1.51j8). Initially, the scale was set in the software and then the thickness of ten layers was measured individually using the line and ROI manager tools in ImageJ software. Mean and standard deviation values of each layer thickness were determined. The theoretical layer thickness was calculated as follows and then compared with the measured layer thickness values.

Total number of layers in PLA/TPU filament

$= 2^{n+1} + 1 = 2^{6+1} + 1 = 129$ (n= number of multipliers, six is used as an example)

Diameter of co-extruded PLA/TPU filament cross-section

= 1.75 mm

Thickness of each layer in the PLA/TPU filament cross-section

= 1.75 mm/129= 13.6 µm

After printing the diameter of PLA/TPU filament reduces from 1.75 to 0.4 mm that is the nozzle diameter of the Flash Forge Creator Pro 3D printer, thereby reducing the diameter of each layer by 4.375 times.

Estimated each layer thickness after printing

= 13.6/4.375= 3.1 µm

Law of Mixtures Calculation: E_1 is the Young's Modulus of the composite material, with E_f and V_f are Young's modulus and volume fraction of PLA while E_m and V_m are Young's modulus and volume fraction of used TPU, respectively.

$$E_1 = E_f V_f + E_m V_m$$
$$= 1046 \times 10^6 \times 0.5 + 1.98 \times 10^6 \times 0.5 \quad (1)$$
$$= 5.24 \times 10^6 \text{ Pa}$$

Cell Culture: NRCM were isolated from 1–2 days old rat pups. The protocol used was approved by the Monash University Animal Ethics Committee and conform to the Australian National Health and Medical Research Council code of practice for the use of animals for scientific purposes. Following the protocol of Ackers-Johnson,[48] three pups were rapidly decapitated, the heart isolated and placed in ice-cold Hank's balanced salt solution (HBSS). The aorta was clamped, and the heart was perfused with solution delivered via a 30 g needle in the left ventricle for 5–7 min to remove all blood. This solution was discarded and the heart was perfused via the ventricle with HBSS containing collagenase (1.5 mg mL^{-1}) and protease XIV (0.05 mg mL^{-1}) for 5–7 min. Perfusion

© 2023 The Authors. Advanced Functional Materials published by Wiley-VCH GmbH

16163028, 0, Downloaded from https://onlinelibrary.wiley.com/doi/10.1002/adfm.202301547 by Cochrane France, Wiley Online Library on [18/04/2023]. See the Terms and Conditions (https://onlinelibrary.wiley.com/terms-and-conditions) on Wiley Online Library for rules of use; OA articles are governed by the applicable Creative Commons License

was stopped and the ventricles were cut into ≈1 mm^3 pieces and incubated at 37 °C for 10 min. Digestion was stopped by the addition of fetal calf serum (FCS) to the solution to achieve a final concentration of 10%. The tissue was gently triturated, and the solution filtered through a 100 µm cell strainer. This procedure used sterile instruments and solutions.

The solution was centrifuged at 250 g for 3 min and the solution removed and replaced by Dulbecco's modified Eagle's medium (DMEM-F-12) without calcium. Calcium was then increased to 2 mM via 0.5 mM/30 min over 2hr. Cells in DMEM-F12 containing 2 mM calcium, 5% FCS, 1% insulin, and 2% bovine serum albumin were seeded at 3×10^5 cells cm^{-2} onto sterilized samples.

24 well plates were used for this cell culture experiment. 24 h later, when cells had adhered to the substrate, half of the medium was replaced to remove any dead or floating cells. The harvested cells consisted of a mixed population of NRCM and fibroblasts, with a high NRCM percentage. A mixed NRCM and fibroblasts population mimics the natural heart environment. All cell culture reagents were acquired from Invitrogen (Mulgrave, Australia) unless specified.

NRCMs were cultured on glass coverslips, PLA, TPU, 1× PLA/TPU, 3× PLA/TPU, and 6× PLA/TPU for 3 days. At this time, they were loaded with the calcium indicator Fluo-4 AM (3 µM, Invitrogen, CA, USA) for 15 min at 37 °C. All image acquisition experiments were carried out at RT, as previously described.[49] Fluorescence images were captured on a confocal microscope (IX71, Olympus) using a 10× objective, passed through a Yokogawa CSU22 Nipkow spinning disc (Yokogawa Australia Pty. Ltd., Macquarie Park, New South Wales, Australia) to a high-sensitivity electron-multiplying Andor iXon CCD camera (Andor Technology PLC, Belfast, N. Ireland). Fluorescence images were acquired every 45 ms, and pixel intensities were analyzed using Andor iQ 1.9 controller software (Andor). Fluorescence responses were corrected for basal fill (F/F_0). Image analysis of the Ca^{2+} signals was in terms of time-dependent changes in mean fluorescence within a user-defined area (25 pixels or 16 µm diameter circle region of interest (ROI)). The LC–Pro plugin for NIH ImageJ software (National Institutes of Health, Bethesda, MD, USA) was utilized as a validated automated ROI detection algorithm solution to Ca^{2+} signal transient detection. This algorithm identifies sites of dynamic Ca^{2+} change above statistical ($p < 0.05$) noise and analysis ROIs encompassing Ca^{2+} transients in 2D time-lapse image sequences.[50]

After Ca^{2+} imaging, the samples with cells still attached were immediately fixed in 4% PFA for immunocytochemistry. The cells were washed, permeabilized, blocked, and incubated in primary antibody overnight at 4 °C on a 45 RPM rocker. Immunocytochemistry staining of NRCM (cardiac troponin T (mouse anti-cardiac troponin T antibody, Abcam, ab33589, 1:500 dilution), connexin 43 (rabbit anti-connexin 43 / GJA1 antibody–intercellular junction marker, Abcam, ab11370, 1:250 dilution), and fibroblasts vimentins (rabbit anti- vimentin Abcam ab45939 antibody–cytoskeleton marker, Abcam at 1:500 dilution) was carried out. The following day, the cells were washed four times with Tween buffer 5 min before incubation in secondary antibody mouse Alexa 488, green (1:1000 dilution) and rabbit Alexa 568, red (1:1000 dilution) for 1.5 h at room temperature. After washing once with PBS, the cells were incubated in 4′,6-diamidino-2-phenylindole (DAPI) (1 µL/5 mL PBS) at room temperature for 5 min to stain nuclei. The cells were washed with PBS three times (5 min each), mounted in DAKO. The slides were stored at 4 °C overnight before imaging using a Nikon Eclipse confocal microscope with excitation lasers at 405 nm (blue for DAPI), 488 nm (green for cardiac troponin T), and 561 nm (red for Connexin 43 and Vimentin) and a 20× oil-immersion objective.[49]

Morphology, shape, dimensions, coverage percentage, and number of NRCMs were determined using CellProfiler 4.0.5, which was a free, open-source software developed by Anne et al., available from the Broad Institute website.[51] First, the ND2 images captured using confocal microscope were converted to separate channels in grey scale .tiff images and combined colored images Figure S10 (Supporting Information). Then, a binary mask image was manually created using Paint 3D over all color images—with white signifying regions in-focus and black for regions out-of-focus. This binary mask image was required to remove the out-of-focus regions, which might skew the measurements.

Figure S11(Supporting Information) illustrates the main pipeline. The greyscale channel .tiff images from Figure S10 (Supporting Information) and manually created binary mask image are the input for the final pipeline to measure the cell features. The UnmixColor module was used to segregate NRCMs and fibroblast nuclei from auto-fluorescent TPU. Fibroblast nuclei are then excluded by setting a pixel diameter limit in the IdentifyPrimaryObject module. This identified NRCM nuclei objects are later utilised as a reference point in the IdentifySecondaryObject module to select the actin filament objects. The MeasurementObjectSizeShape module was used to determine the size of NRCMs actin filament features, and finally ExportToSpreadsheet module was used to export these measurements as a cvs file, which was compared using GraphPad Prism 8.

The eccentricity (elongation), minor axis length, major axis length, minimum, and maximum ferret diameter values of NRCMs were determined using CellProfiler.[51] The eccentricity is the ratio of the distance between the foci of the ellipse and its major axis length. The value is between 0 and 1 with 0 being a perfect circle and 1 is an ellipse. The length (in pixels) of the major axis of the ellipse is called as the major axis length and the length (in pixels) of the minor axis of the ellipse is defined as minor axis length. The feret diameter is the distance between two parallel lines tangent on either side of the measured object, similar to taking a caliper measurement of an object at various angles. The minimum and maximum feret diameters are defined as the smallest and largest possible diameters, determined by rotating the calipers at all possible angles.

After 3 days, cells on the 3D printed samples (not the same cells used for calcium imaging or IHC) were fixed with Karnovsky fixative for 2 h, washed thrice with PBS, and postfixed with 1% osmium tetroxide for 1 h at room temperature. The samples were washed thrice with milliQ water (10 min each). Dehydration was achieved using a series of ethanol washes (50%, 60%, 70%, 80%, 90%, 95%, and 100%) followed by twice hexamethyldisilane (HMDS) drying procedure (10 min each). Finally, the specimens were sputter-coated with gold for 120 sec to achieve a 20 nm gold coating thickness and subsequently imaged using FEI Nova NanoSEM.

Supporting Information

Supporting Information is available from the Wiley Online Library or from the author.

Acknowledgements

The authors would like to thank Monash University for a Monash Graduate Scholarship award, a Monash International Postgraduate Research Scholarship, and a Graduate Research International Travel Award (to MVV). The authors would also like to thank the Australasian Society for Biomaterials and Tissue Engineering (ASBTE) for the award of International Lab Travel Award (to MVV). The authors acknowledge the use of instruments, and scientific and technical assistance at the Monash Centre for Electron Microscopy, a Node of Microscopy Australia, the Monash Micro Imaging Platform and the Ramaciotti Centre for Structural Cryo-Electron Microscopy.

Open access publishing facilitated by Monash University, as part of the Wiley - Monash University agreement via the Council of Australian University Librarians.

Conflict of Interest

The authors declare no conflict of interest.

© 2023 The Authors. Advanced Functional Materials published by Wiley-VCH GmbH

16163028, 0, Downloaded from https://onlinelibrary.wiley.com/doi/10.1002/adfm.202301547 by Cochrane France, Wiley Online Library on [18/04/2023]. See the Terms and Conditions (https://onlinelibrary.wiley.com/terms-and-conditions) on Wiley Online Library for rules of use; OA articles are governed by the applicable Creative Commons License

Data Availability Statement

The data that support the findings of this study are available from the corresponding author upon reasonable request.

Keywords

additive manufacturing, architectured materials, biomaterials, co-extrusion

Received: February 9, 2023
Revised: March 14, 2023
Published online:

[1] M. Ashby, *Scr. Mater.* **2013**, *68*, 4.
[2] a) J. W. C. Dunlop, P. Fratzl, *Annu. Rev. Mater. Res.* **2010**, *40*, 1; b) B. Wang, W. Yang, J. McKittrick, M. A. Meyers, *Prog. Mater. Sci.* **2016**, *76*, 229.
[3] a) M. F. Ashby, Y. J. M. Bréchet, *Acta Mater.* **2003**, *51*, 5801; b) P. M. Weaver, M. F. Ashby, *J. Eng. Design* **1996**, *7*, 129; c) S. E. Naleway, M. M. Porter, J. McKittrick, M. A. Meyers, *Adv. Mater.* **2015**, *27*, 5455; d) P. Fratzl, O. Kolednik, F. D. Fischer, M. N. Dean, *Chem. Soc. Rev.* **2016**, *45*, 252; e) G. M. Luz, J. F. Mano, *Philos. Trans. R. Soc., A* **2009**, *367*, 1587; f) E. Munch, M. E. Launey, D. H. Alsem, E. Saiz, A. P. Tomsia, R. O. Ritchie, *Science* **2008**, *322*, 1516.
[4] a) M. O. Al-Barqawi, B. Church, M. Thevamaran, D. J. Thoma, A. Rahman, *Materials* **2022**, *15*, 3310; b) G. Cidonio, M. Glinka, J. I. Dawson, R. O. C. Oreffo, *Biomaterials* **2019**, *209*, 10.
[5] a) A. Kramschuster, L. S. Turng, *J. Biomed. Mater. Res., Part B* **2010**, *92B*, 366; b) M. Hou, Q. Wu, M. Dai, P. Xu, C. Gu, X. Jia, J. Feng, X. Mo, *Biomed. Mater.* **2014**, *10*, 015005; c) A. Lis-Bartos, A. Smieszek, K. Frańczyk, K. Marycz, *Polymers* **2018**, *10*, 1073; d) S. K. Dogan, S. Boyacioglu, M. Kodal, O. Gokce, G. Ozkoc, *J. Mech. Behav. Biomed. Mater.* **2017**, *71*, 349; e) J. Nakamatsu, F. G. Torres, O. P. Troncoso, Y. Min-Lin, A. R. Boccaccini, *Biomacromolecules* **2006**, *7*, 3345; f) L. Wang, J. Shi, L. Liu, E. Secret, Y. Chen, *Microelectron. Eng.* **2011**, *88*, 1718; g) S. A. Park, H. J. Kim, S. H. Lee, J. H. Lee, H. K. Kim, T. R. Yoon, W. Kim, *Polym. Eng. Sci.* **2011**, *51*, 1883; h) Y. M. Corre, A. Maazouz, J. Duchet, J. Reignier, *J. Supercrit. Fluids* **2011**, *58*, 177; i) H. B. Wu, H. J. Haugen, E. Wintermantel, *J. Cell. Plast.* **2011**, *48*, 141; j) R. Guo, S. Lu, J. M. Page, A. R. Merkel, S. Basu, J. A. Sterling, S. A. Guelcher, *Adv. Healthcare Mater.* **2015**, *4*, 1826; k) Q. Chen, J. D. Mangadlao, J. Wallat, A. De Leon, J. K. Pokorski, R. C. Advincula, *ACS Appl. Mater. Interf.* **2017**, *9*, 4015; l) S. Murugan, S. R. Parcha, *J Mater Sci Mater Med* **2021**, *32*, 93.
[6] A. Dey, I. N. Roan Eagle, N. Yodo, *J. Manuf. Mater. Process.* **2021**, *5*, 69.
[7] a) P. Parandoush, D. Lin, *Compos. Struct.* **2017**, *182*, 36; b) G. D. Goh, Y. L. Yap, S. Agarwala, W. Y. Yeong, *Adv. Mater. Technol.* **2019**, *4*, 1800271; c) K. Gnanasekaran, T. Heijmans, S. van Bennekom, H. Woldhuis, S. Wijnia, G. de With, H. Friedrich, *Appl. Mater. Today* **2017**, *9*, 21; d) J. G. Siqueiros, K. Schnittker, D. A. Roberson, *Virtual Phys. Prototyping* **2016**, *11*, 123.
[8] a) Z. Jiao, B. Luo, S. Xiang, H. Ma, Y. Yu, W. Yang, *Adv. Ind. Eng. Polym. Res.* **2019**, *2*, 196; b) M. Kim, J. H. Jeong, J. Y. Lee, A. Capasso, F. Bonaccorso, S. H. Kang, Y. K. Lee, G. H. Lee, *ACS Appl. Mater. Interf.* **2019**, *11*, 11841; c) X. Wang, M. Jiang, Z. Zhou, J. Gou, D. Hui, *Compos. Part B* **2017**, *110*, 442.
[9] a) Z. Li, A. Olah, E. Baer, *Prog. Polym. Sci.* **2020**, *102*, 101210; b) T. Messin, N. Follain, A. Guinault, C. Sollogoub, V. Gaucher, N. Delpouve, S. Marais, *ACS Appl. Mater. Interf.* **2017**, *9*, 29101.
[10] a) J. Kerns, A. Hsieh, A. Hiltner, E. Baer, *Macromol. Symp.* **1999**, *147*, 15; b) T. Alfrey, Jr., E. F. Gurnee, W. J. Schrenk, *Polym. Eng. Sci.* **1969**, *9*, 400; c) H. Wang, J. K. Keum, A. Hiltner, E. Baer, B. Freeman, A. Rozanski, A. Galeski, *Science* **2009**, *323*, 757.
[11] A. Bironeau, J. Dirrenberger, C. Sollogoub, G. Miquelard-Garnier, S. Roland, *J Microsc* **2016**, *264*, 48.
[12] J. Carthew, J. B. J. Taylor, M. R. Garcia-Cruz, N. Kiaie, N. H. Voelcker, V. J. Cadarso, J. E. Frith, *ACS Appl. Mater. Interfaces* **2022**, *14*, 23066.
[13] E. L. Gilmer, D. Miller, C. A. Chatham, C. Zawaski, J. J. Fallon, A. Pekkanen, T. E. Long, C. B. Williams, M. J. Bortner, *Polymer* **2018**, *152*, 51.
[14] a) F. Fei, Y. Lin, *J. Appl. Polym. Sci.* **2011**, *119*, 2778; b) J.-J. Han, H.-X. Huang, *J. Appl. Polym. Sci.* **2011**, *120*, 3217.
[15] a) H. Y. Mi, M. R. Salick, X. Jing, B. R. Jacques, W. C. Crone, X. F. Peng, L. S. Turng, *Mater. Sci. Eng., C* **2013**, *33*, 4767; b) Y. H. Lee, B. K. Kang, H. D. Kim, H. J. Yoo, J. S. Kim, J. H. Huh, Y. J. Jung, D. J. Lee, *Macromol. Res.* **2009**, *17*, 616.
[16] a) A. S. Khan, Z. Ahmed, M. J. Edirisinghe, F. S. L. Wong, I. U. Rehman, *Acta Biomater.* **2008**, *4*, 1275; b) H. Janik, B. Palys, Z. S. Petrovic, *Macromol. Rapid Commun.* **2003**, *24*, 265; c) S. Parnell, K. Min, M. Cakmak, *Polymer* **2003**, *44*, 5137.
[17] G. Kister, G. Cassanas, E. Fabrègue, L. Bardet, *Eur. Polym. J.* **1992**, *28*, 1273.
[18] D. Langhe, M. Ponting, *Manufacturing and Novel Applications of Multilayer Polymer Films*, William Andrew Publishing, Boston **2016**.
[19] S. K. Dogan, E. A. Reyes, S. Rastogi, G. Ozkoc, *J. Appl. Polym. Sci.* **2014**, 131.
[20] R. S. Porter, L. H. Wang, *Polymer* **1992**, *33*, 2019.
[21] N. M. Nordin, Y. F. Buys, H. Anuar, M. H. Ani, M. M. Pang, *Mater Today Proc* **2019**, *17*, 500.
[22] T. Yao, J. Ye, Z. Deng, K. Zhang, Y. Ma, H. Ouyang, *Compos B Eng* **2020**, *188*, 107894.
[23] a) P. Pandey, W. Hawkes, J. Hu, W. V. Megone, J. Gautrot, N. Anilkumar, M. Zhang, L. Hirvonen, S. Cox, E. Ehler, J. Hone, M. Sheetz, T. Iskratsch, *Dev. Cell* **2018**, *44*, 326; b) I. Batalov, Q. Jallerat, S. Kim, J. Bliley, A. W. Feinberg, *Sci. Rep.* **2021**, *11*, 11502; c) A. Ul Haq, F. Carotenuto, F. De Matteis, P. Prosposito, R. Francini, L. Teodori, A. Pasquo, P. Di Nardo, *Int. J. Mol. Sci.* **2021**, 22.
[24] G. del Monte-Nieto, J. W. Fischer, D. J. Gorski, R. P. Harvey, J. C. Kovacic, *J Am Coll Cardiol* **2020**, *75*, 2169.
[25] a) S. Spinella, C. Samuel, J. M. Raquez, S. A. McCallum, R. Gross, P. Dubois, *ACS Sustainable Chem. Eng.* **2016**, *4*, 2517; b) P. Król, B. Król, *Colloid Polym. Sci.* **2012**, *290*, 879.
[26] K. Park, H. Jeong, *J. Electrochem. Soc.* **2008**, *155*, H595.
[27] S. Cai, C. Wu, W. Yang, W. Liang, H. Yu, L. Liu, *Nanotechnol. Rev.* **2020**, *9*, 971.
[28] T. Trantidou, E. J. Humphrey, C. Poulet, J. Gorelik, T. Prodromakis, C. M. Terracciano, *Tissue Eng., Part C: Methods* **2016**, *22*, 464.
[29] L. Qi, E. K. Knapton, X. Zhang, T. Zhang, C. Gu, Y. Zhao, *Sci. Rep.* **2017**, *7*, 8361.
[30] Y. Arima, H. Iwata, *Biomaterials* **2007**, *28*, 3074.
[31] J. Wei, M. Yoshinari, S. Takemoto, M. Hattori, E. Kawada, B. Liu, Y. Oda, *J Biomed Mater Res B Appl Biomater* **2007**, *81B*, 66.
[32] P. Davidson, M. Bigerelle, G. Reiter, K. Anselme, *Biointerphases* **2015**, *10*, 031004.
[33] M. Viola, S. Piluso, J. Groll, T. Vermonden, J. Malda, M. Castilho, *Adv. Healthcare Mater.* **2021**, *10*, 2101021.
[34] P. Kuo, H. Lee, M. A. Bray, N. A. Geisse, Y. T. Huang, W. J. Adams, S. P. Sheehy, K. K. Parker, *Am. J. Pathol.* **2012**, *181*, 2030.
[35] T. Pong, W. J. Adams, M. A. Bray, A. W. Feinberg, S. P. Sheehy, A. A. Werdich, K. K. Parker, *Exp. Biol. Med. (Maywood, N.J.)* **2011**, *236*, 366.
[36] F. Zhang, N. Zhang, H. X. Meng, H. X. Liu, Y. Q. Lu, C. M. Liu, Z. M. Zhang, K. Y. Qu, N. P. Huang, *ACS Biomater. Sci. Eng.* **2019**, *5*, 3022.

© 2023 The Authors. Advanced Functional Materials published by Wiley-VCH GmbH

16163028, 0, Downloaded from https://onlinelibrary.wiley.com/doi/10.1002/adfm.202301547 by Cochrane France, Wiley Online Library on [18/04/2023]. See the Terms and Conditions (https://onlinelibrary.wiley.com/terms-and-conditions) on Wiley Online Library for rules of use; OA articles are governed by the applicable Creative Commons License

[37] C. Zhu, A. E. Rodda, V. X. Truong, Y. Shi, K. Zhou, J. M. Haynes, B. Wang, W. D. Cook, J. S. Forsythe, *ACS Biomater. Sci. Eng.* **2018**, *4*, 2494.
[38] P. Haftbaradaran Esfahani, Z. ElBeck, S. Sagasser, X. Li, M. B. Hossain, H. A. Talukdar, R. Sandberg, R. Knöll, *Basic Res. Cardiol.* **2019**, *115*, 7.
[39] I. Boutin-Ganache, S. Picard, C. F. Deschepper, *Physiol Genomics* **2002**, *12*, 61.
[40] V. Robert, P. Gurlini, V. Tosello, T. Nagai, A. Miyawaki, F. Di Lisa, T. Pozzan, *EMBO J.* **2001**, *20*, 4998.
[41] P. Kuo, H. Lee, M. Bray, N. A. Geisse, Y. Huang, W. J. Adams, S. P. Sheehy, K. K. Parker, *Am. J. Pathol.* **2012**, *181*, 2030.
[42] B. E. Dabiri, H. Lee, K. K. Parker, *Prog Biophys Mol Biol* **2012**, *110*, 196.
[43] M. L. McCain, K. K. Parker, *Pflugers Arch* **2011**, *462*, 89.
[44] N. Tsuji, Y. Saito, S. H. Lee, Y. Minamino, *Adv. Eng. Mater.* **2003**, *5*, 338.
[45] a) H. P. Ng, T. Przybilla, C. Schmidt, R. Lapovok, D. Orlov, H. W. Höppel, M. Göken, *Mater. Sci. Eng., Proc. Conf.* **2013**, *576*, 306; b) M. Eizadjou, A. Kazemi Talachi, H. Danesh Manesh, H. Shakur Shahabi, K. Janghorban, *Compos. Sci. Technol.* **2008**, *68*, 2003.
[46] Y. Beygelzimer, R. Kulagin, P. Fratzl, Y. Estrin, *Adv. Mater.* **2021**, *33*, 2005473.
[47] S. El Habnouni, V. Darcos, X. Garric, J. P. Lavigne, B. Nottelet, J. Coudane, *Adv. Funct. Mater.* **2011**, *21*, 3321.
[48] M. Ackers-Johnson, P. Y. Li, A. P. Holmes, S. M. O'Brien, D. Pavlovic, R. S. Foo, *Circ. Res.* **2016**, *119*, 909.
[49] J. B. Marroquin, H. A. Coleman, M. A. Tonta, K. Zhou, B. Winther-Jensen, J. Fallon, N. W. Duffy, E. Yan, A. A. Abdulwahid, J. J. Jasieniak, J. S. Forsythe, H. C. Parkington, *Adv. Funct. Mater.* **2018**, *28*, 1700927.
[50] M. Francis, J. Waldrup, X. Qian, M. S. Taylor, *J. Vis. Exp.* **2014**, *5*, 447.
[51] A. E. Carpenter, T. R. Jones, M. R. Lamprecht, C. Clarke, I. H. Kang, O. Friman, D. A. Guertin, J. H. Chang, R. A. Lindquist, J. Moffat, P. Golland, D. M. Sabatini, *Genome Biol.* **2006**, *7*, R100.

© 2023 The Authors. Advanced Functional Materials published by Wiley-VCH GmbH

16163028, 0, Downloaded from https://onlinelibrary.wiley.com/doi/10.1002/adfm.202301547 by Cochrane France, Wiley Online Library on [18/04/2023]. See the Terms and Conditions (https://onlinelibrary.wiley.com/terms-and-conditions) on Wiley Online Library for rules of use; OA articles are governed by the applicable Creative Commons License